Journal of Nuclear Materials 587 (2023) 154755

Contents lists available at ScienceDirect

Journal of Nuclear Materials

journal homepage: www.elsevier.com/locate/jnucmat

# Experimental and modelling evidence for hydrogen trapping at a β-Nb second phase particle and Nb-rich nanoclusters in neutron-irradiated low Sn ZIRLO

Benjamin M. Jenkins [a,b,*], Jack Haley [a,c], Lucia Chen [d], Baptiste Gault [e,f], Patrick A. Burr [d], Anne Callow [a], Michael P. Moody [a], Christopher R.M. Grovenor [a]

[a] Department of Materials, University of Oxford, Parks Road, Oxford OX1 3PH, UK
[b] University of Rouen Normandy, CNRS, INSA Rouen Normandie, Groupe de Physique des Matériaux UMR 6634, F-76000 Rouen, France
[c] UKAEA, Culham Science Centre, Abingdon, Oxfordshire OX14 3DB, UK
[d] School of Mechanical and Manufacturing Engineering, UNSW Sydney, Sydney, Australia
[e] Max-Planck-Institut für Eisenforschung, Max-Planck-Straße 1, Düsseldorf, Germany
[f] Department of Materials, Royal School of Mines, Imperial College London, London, UK

ARTICLE INFO

*Keywords:*
Atom probe tomography (APT)
Zirconium fuel cladding
Hydrogen embrittlement
Cryo-FIB
Second phase particles

ABSTRACT

Zirconium-based alloys used for fuel cladding in nuclear fission reactors are susceptible to hydrogen embrittlement during operation, but we currently lack the necessary mechanistic understanding of how hydrogen behaves in the materials during service to properly address this issue. Imaging the distribution of hydrogen within material microstructures is key to creating or validating models that predict the behaviour and influence of hydrogen on material properties, but is experimentally difficult. Studying hydrogen in zirconium-alloys is further complicated by the fact that the most common routes for preparing specimens for Transmission Electron Microscopy and Atom Probe Tomography (APT) analysis, electropolishing and focused ion beam (FIB) milling, are known to induce hydride formation. This introduces uncertainty as to whether the hydrogen distribution in the analysed specimen is actually representative of the entire sample a priori. Recent work has shown that this effect can be mitigated by performing the final specimen thinning stages at cryogenic temperatures. In this paper we use cryo-FIB to prepare APT specimens of neutron-irradiated low Sn ZIRLO, showing that hydrogen is trapped within a β-Nb SPP and at Nb-rich nanoclusters formed by exposure to neutron irradiation. We then use density functional theory calculations to explain these experimental observations. These results highlight the importance of including niobium-rich features in models used to predict hydrogen pick-up in zirconium alloys during service and delayed hydride cracking during storage.

## 1. Introduction

Zr-based alloys are used for fuel cladding in light water nuclear reactors, but are known to suffer from hydrogen pick-up and embrittlement during service, and delayed hydride cracking (DHC) during storage. The oxidation of Zr metal during exposure to water or steam results in the production of free atomic hydrogen, which can then diffuse into the metal [1]. As corrosion of the Zr continues during service, the levels of hydrogen will also gradually increase, with, for instance, hydrogen contents of ~100 wt. ppm measured in ZIRLO after 240 days of exposure to corrosive environments [2]. This pick-up of hydrogen during service can result in the formation of hydrides upon cooling, as the solubility limit of hydrogen in α-Zr is exceeded [3,4]. Corrosion of the cladding during service can also necessitate replacement of the fuel assembly as the hydrogen content approaches critical levels. In order to predict the safe service lifetime before critical hydrogen levels are reached in the matrix, and DHC evolution during storage, it is necessary to understand how the hydrogen content and hydride fraction evolves over time and thermal history [5,6]. This evolution will be impacted by both the hydrogen pickup rate and the trapping efficiency of microstructural features such as second phase particles (SPPs) or irradiation-induced dislocation loops [7].

* Corresponding author.
*E-mail address:* benjamin.jenkins@materials.ox.ac.uk (B.M. Jenkins).

https://doi.org/10.1016/j.jnucmat.2023.154755
Received 10 April 2023; Received in revised form 25 September 2023; Accepted 25 September 2023
Available online 27 September 2023

Experimentally observing the location of hydrogen present in microstructures remains challenging, and predictions from computational modelling are frequently relied upon to identify potential trapping sites. Modelling studies in Zr have indicated that hydrogen is likely to show, compared to the α-Zr matrix, increased thermodynamic stability at some SPPs [8,9]. The strength of this effect is thought to be dependant upon the chemical composition of the SPPs. For example, Tuli et al. found a positive correlation between hydrogen trapping strength and the Zr content in the β-(Zr,Nb) phase, suggesting that β-Zr may be a relatively strong sinks for hydrogen while β-Nb is predicted to have a similar affinity as the α-Zr matrix [9]. Increasing the Cr:Fe ratio of $Zr(Cr,Fe)_2$ SPPs, and the Nb:Fe ratio of $Zr(Nb,Fe)_2$ SPPs is also expected to increase the likelihood of hydrogen being trapped [8,10]. However, the majority of these predictions are yet to be confirmed experimentally.

Jones et al. have observed increased levels of deuterium ($^2$H) around SPPs using nanoscale secondary ion mass spectrometry (NanoSIMS) after exposing Zr-based metal alloys to heavy water in an autoclave environment [10]. The authors claim that the $^2$H is trapped at the interface between the α-Zr matrix and Fe and Cr-rich SPPs, although some NanoSIMS maps indicate that $^2$H levels are also enriched within specific SPPs.

Due to the small sizes of the potential hydrogen trapping sites in Zr alloys, it is necessary to use characterisation techniques with high spatial and chemical resolution. Atom probe tomography (APT) is such a technique, and a potentially powerful route for investigating the trapping behaviour of hydrogen [11–15], and the early stages of hydride formation [16,17].

However, imaging either hydrides or trapped hydrogen in Zr alloys with APT is complicated by the fact that both electropolishing and focused ion beam (FIB) preparation of samples is known to induce hydride formation in hexagonal close packed (HCP) materials [18–20]. Avoiding the introduction of hydrogen into samples during sample preparation is crucial if a true understanding of the behaviour of hydrogen in a complex microstructure is to be achieved. Hanlon et al. have shown that the aforementioned effect can be mitigated in Zr alloys by performing the final FIB preparation stages of transmission electron microscopy (TEM) foils at cryogenic temperatures [21]. More recently, Mouton et al. demonstrated that the use of cryo-FIB can prevent spurious hydride formation whilst preparing APT specimens [5], and Mayweg et al. have recently shown that cryo-FIB significantly reduces but does not entirely remove hydrogen pick-up during FIB preparation [22]. Therefore, the use of cryo-FIB to prepare APT specimens from a neutron-irradiated Zr alloy provides the opportunity to study the real behaviour of hydrogen in the microstructure after in-reactor irradiation.

Here, we present APT data of a neutron-irradiated low Sn ZIRLO alloy prepared using FIB at cryogenic temperatures. Our results show that increased levels of hydrogen are associated with β-Nb SPPs and at Nb-rich nanoclusters. Density functional theory (DFT) modelling is used to rationalise these observations and reveals that hydrogen is likely to be trapped at these sites. The trapping of hydrogen at Nb features in Nb-containing Zr alloys may impact the service lifetime at which the critical hydrogen content for hydride formation is reached in the matrix, and should also be accounted for in models predicting DHC.

## 2. Materials and methods

### 2.1. Materials

The composition of the Nb-containing low Sn ZIRLO alloy used in this study is shown in Table 1. The manufacturing route and heat treatment applied to each alloy has been previously reported in [23,24].

**Table 1**
Nominal composition (wt.%) of the low Sn ZIRLO alloy analysed in this study.

| Alloy | Nb | Sn | Fe | Ni | Cr | O |
|---|---|---|---|---|---|---|
| Low Sn ZIRLO | 0.95 | 0.66 | 0.12 | 0.0036 | 0.0073 | 0.12 |

The alloy was neutron-irradiated in the BOR-60 reactor at 320 ± 10 °C up to a fluence of $2.1 \times 10^{25}$ n/m$^2$ [24], which corresponds to a damage level of around 3 dpa.

### 2.2. Experimental methods

Aside from the use of cryogenic temperatures, conventional FIB-based APT sample preparation procedures were followed [25–27]. Specimens were prepared in two stages using FIB. Initial milling and lift-outs were performed using FIB at ambient temperatures using a FEI Helios NanoLab 600i $Ga^+$ ion FIB before undergoing final sample thinning at −90 °C. A final FIB polishing stage was also performed at −90 °C using an accelerating voltage of 2 kV and a beam current of 190 pA in an attempt to limit any Ga+ damage.

APT analyses were conducted on a Cameca LEAP 5000-XR at the University of Oxford's Nuclear Materials Atom Probe (NuMAP) Facility; the analysis conditions for individual datasets will be specified in figure captions and in the text, where appropriate. Reconstructions and analyses were performed in IVAS 3.8.8. AtomProbeLab, which solves peak overlaps and decomposes complex ions into their constituent atomic species, was used for compositional calculations [28,29].

### 2.3. Density function theory modelling methodology

DFT modelling was carried out to increase our understanding of the interaction of hydrogen with the Nb-rich nanoclusters that form under irradiation. The nanoclusters were modelled as disordered hexagonally close packed (HCP) solid solutions, with a composition similar to that determined from the APT data, as discussed later. The simulations were conducted using DFT with a 150-atom special quasi-random structure (SQS), comprising a 5 × 5 × 3 supercell of the conventional HCP-Zr unit cell. The SQS was generated using the MCSQS code [30] with pair, triplet, and quadruplet correlations defined up to the sixth, fourth, and second nearest neighbour shells, respectively. The atomic positions in the resultant SQS were relaxed with the Vienna Ab-initio Simulation Package VASP [31], where the lattice parameters of the SQS were calculated using Vegard's Law from the relaxed DFT lattice parameters of the end members.

A single hydrogen atom was placed in each of the 300 tetrahedral interstitial sites in the SQS, and the atomic positions were further relaxed. The trapping energy was defined as the relative change in hydrogen solution energy for hydrogen in an interstitial site ($i$) of the cluster compared to a tetrahedral site in pure α-Zr. This was calculated as

$$\Delta E^{H}_{sol,i} = \left(E^{DFT}_{\mathrm{hcp-Zr}} + E^{DFT}_{cluster+\mathrm{H}_i}\right) - \left(E^{DFT}_{\mathrm{hcp-Zr+H}_i} + E^{DFT}_{cluster}\right)$$

where $E^{DFT}_{\mathrm{hcp-Zr}}$ and $E^{DFT}_{cluster}$ are the DFT energies of pure HCP -Zr and the HCP nanocluster respectively. A subscript $+H_i$ indicates the addition of a hydrogen atom at a tetrahedral interstitial site. Our assumption that the nanoclusters have a HCP structure is discussed below.

All DFT simulations used the Perdew-Burke-Ernzerhof (PBE) functional [32] and a planewave cut-off energy of 350 eV. Brillouin zone sampling was performed with a 3 × 3 × 3 Γ-centred Monkhorst-Pack mesh. Forces and energy differences were converged to $10^{-5}$ eV/Å and $10^{-6}$ eV, respectively, using a Blocked-Davidson algorithm. Bands were smeared to a width of 0.1 eV using a first order Methfessel-Paxton method.

## 3. Results & discussion

### 3.1. Beta-Nb second phase particle

Fig. 1 shows an APT dataset that contains both neutron irradiation-

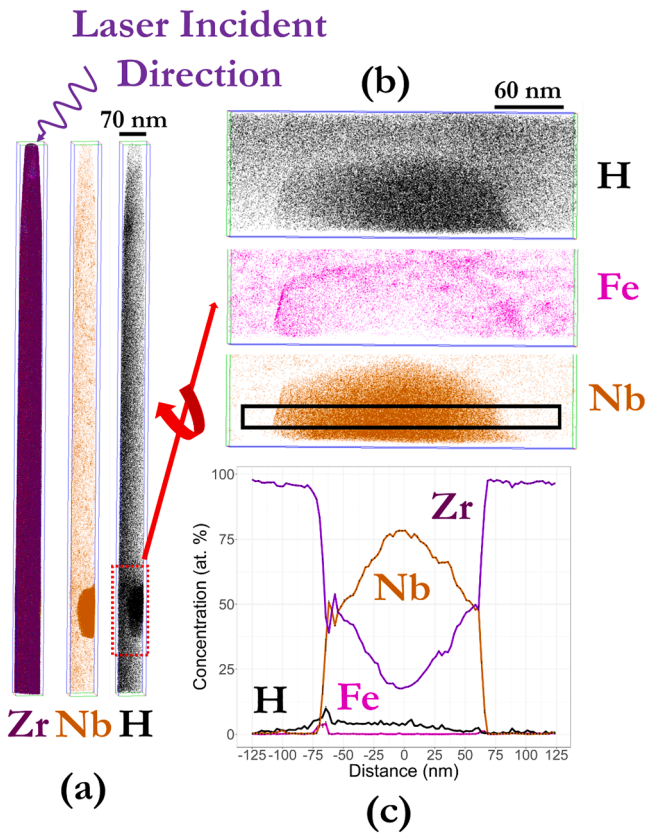


**Fig. 1.** (a) Atom maps of Zr, Nb, and H in low Sn ZIRLO sample irradiated to 3 dpa and prepared via cryo-FIB (bounding box dimensions 70 nm × 72 nm × 1460 nm). (c) Atom maps of H, Fe, and Nb from region of interest highlighted by red box in (a) (bounding box dimensions 70 nm × 72 nm × 300 nm). (d) One-dimensional concentration profile through the region of interest indicated by the black box in (c). Analysis temperature = 60 K, laser pulse energy = 80 pJ. (For interpretation of the references to colour in this figure legend, the reader is referred to the web version of this article.)

induced Nb nanoclusters and a Nb-rich SPP characteristic of the unirradiated microstructure [33,34]. In this Figure and subsequent atom maps, H refers to both $H^+$ and $H_2^+$ ions. The hydrogen concentration in the entire dataset was measured to be 2.42 ± 0.02 at.% and the composition of the SPP away from the interface with the α-Zr matrix is given in Table 2. Whilst cryo-FIB does reduce the amount of hydrogen that is introduced to the sample during preparation [21] it is unlikely to entirely remove it [22]. In addition there are other sources of spurious hydrogen that arise during APT analyses and must be considered when interpreting APT data [35]. Therefore, the reported concentrations of hydrogen, as measured via APT, represent an upper limit to the true content within the material. The composition within the SPP is consistent with that expected of a β-Nb SPP after conventional alloy processing [36].

**Table 2**
Composition of the Nb-rich SPP in Fig. 1. Composition was determined away from the interface with the α-Zr matrix. Error indicates uncertainty due to peak overlap solving.

| Element | Atomic% |
|---|---|
| Zr | 22.81 ± 0.14 |
| Nb | 72.81 ± 0.26 |
| H | 4.31 ± 0.26 |
| O | 0.02 ± 0.02 |
| Fe | 0.03 ± 0.01 |
| Cr | 0.01 ± 0.01 |
| Sn | 0.01 ± 0.01 |

A non-random distribution of hydrogen is clearly visible in the dataset, with a higher density of hydrogen associated with the opposite side of the specimen from the laser incidence, and also within the large Nb-rich SPP on the laser-incident side of the sample. Fig. 2(a) and (b) compare the mass spectra for the laser-incident and non-laser-incident sides of the samples, respectively. Comparison of the charge-state-ratios of $Zr^{3+}/Zr^{2+}$ in these parts of the sample do show a small variation, increasing from 0.002 on the laser-incident side to 0.003 on the non-laser-incident side; this indicates that ion evaporation occurs at a lower field on the laser-incident side of the samples than from the non-laser-incident side. Differences in the electrostatic field across the emitting end of an APT specimen during laser-pulsing experiments have previously been reported [37] and explained as a result of "shadowing" leading to non-uniform illumination and heating of the tip from the laser pulse. This difference in field can explain the observation of more hydrogen in the 1 Da and 2 Da peaks on the non-laser-incident side of the sample vs the laser-incident side, since a reduction in electric field would mean that $H_2$ ions are less likely to decompose into two $H_1$ ions during the field evaporation process [38,39]. The variation in field across the specimen surface also encourages species to migrate over the surface towards regions of high field before undergoing field evaporation [40]. The combination of both these effects leads to the excess hydrogen counts detected on the non-laser-incident side of the specimen in Fig. 1.

In this dataset, the hydrogen content was most concentrated within the β-Nb SPP as is clearly visible in the atom map (Fig. 1(b)). The hydrogen content in the SPP was 4.3 at.% compared to 2.4 at.% in the rest of the analysed volume. A one-dimensional (1D) concentration profile was taken through the SPP along the depth (z) direction, as indicated by the black region of interest in Fig. 1(b), and (c) shows the enrichment of both hydrogen and Nb in the SPP. In Fig. 1(c), Fe was also observed to segregate to the interface between the SPP and Zr matrix as has previously been reported [41,42]. This observation of increased hydrogen in the SPP needs to be discussed in the light of previous modelling work indicating that β-Nb should only act as a weak sink for hydrogen in an α-Zr matrix [8,9].

First, we should consider the accuracy of hydrogen measurements due to the artefacts associated with APT previously described [35,39,43], and it is important to address each of these in turn to assess the validity of our observation of hydrogen segregating to the SPP. The following are possible reasons that may lead to an artificial increase in hydrogen signal being detected during an APT experiment.

1) Hydrogen induced in sample during preparation

As has been demonstrated previously [21,22], holding the sample at cryogenic temperatures while preparing specimens leads to a significant reduction in the levels of hydrogen introduced into the analysed volume. Even if some hydrogen was introduced into this sample during preparation, it does not explain why it is analysed at higher concentration in the SPP than the matrix unless the β-Nb SPPs do act as favourable sinks.

2) Hydrogen in analysis chamber

The majority of APT analysis chambers are made from hydrogen-permeable materials, such as stainless steel, and even using lower outgassing materials like titanium is unable to completely remove hydrogen from the chamber during sample analysis [44]. This gaseous hydrogen is able to adsorb and then dissociate on the sample surface before undergoing field evaporation and being detected in the mass spectrum. It is likely that some of the hydrogen detected in the APT analyses in this study is due to this phenomenon, especially on the non-laser-incident side of the analysed volume in Fig. 1. However, on a theoretically perfect hemispherical apex with uniform field distribution, as above, the only explanation for detecting a higher concentration of hydrogen is if the β-Nb SPPs act as a favourable sink.

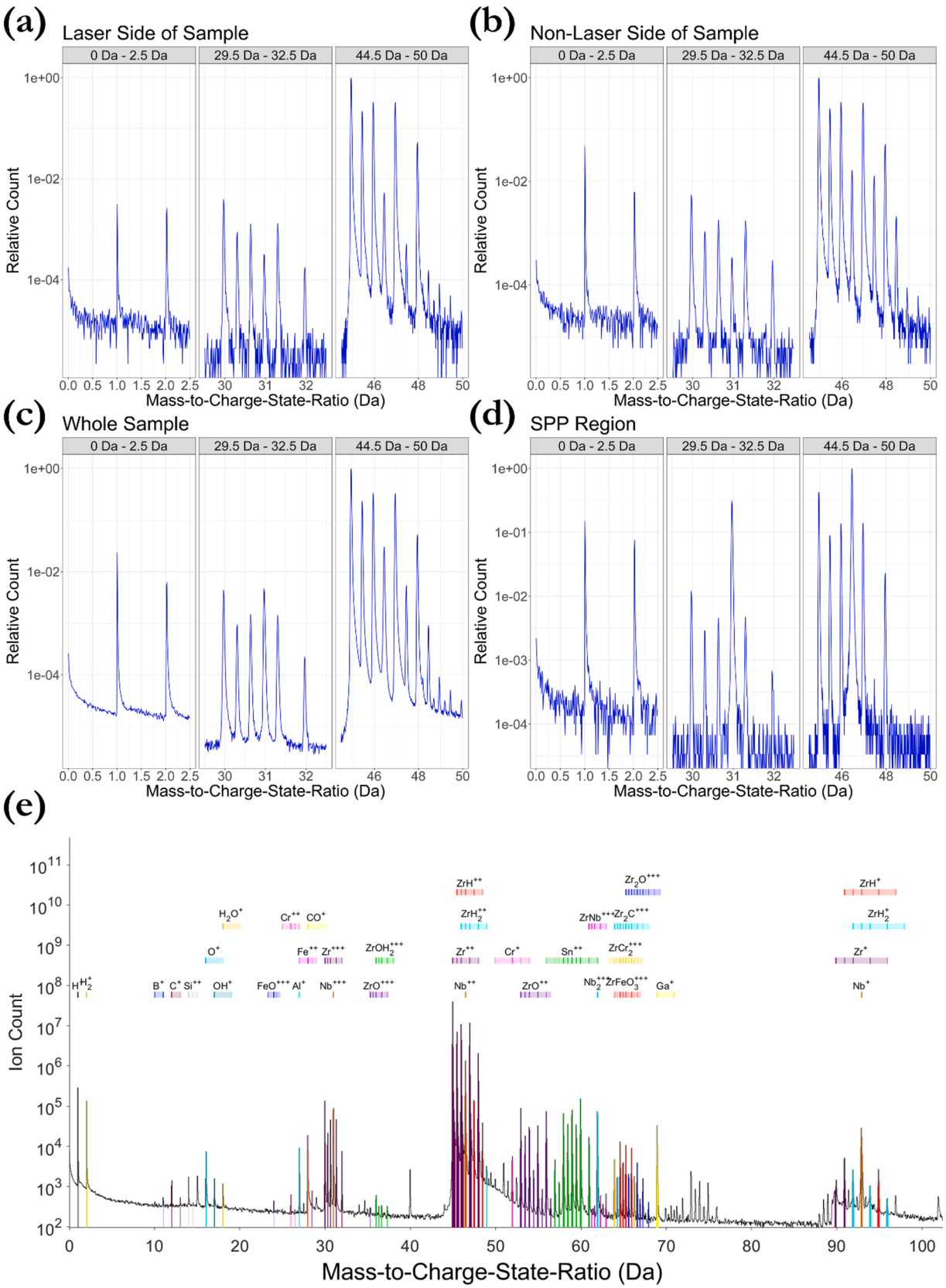


**Fig. 2.** (a)-(d) Relative abundance of the 0–2.5 Da, 29.5–32.5 Da, and 44.5–49.5 Da regions of the APT mass spectrum for different sections of the sample. (e) Global mass spectrum up to 100 Da and ranged ions that were present in the dataset from Fig. 1. Analysis temperature = 60 K, laser pulse energy = 80 pJ.

Nevertheless, the tip is unlikely to remain perfectly hemispherical during the experiment due to the differences in the evaporation fields of Zr and Nb. It is therefore important to address what effect we would expect this to have on detected levels of hydrogen.

3) Difference in evaporation rates due to evaporation fields of Zr and Nb

The evaporation field of pure Nb (37 $Vnm^{-1}$) is calculated to be higher than that of Zr (28 $Vnm^{-1}$) [45]. This should result in the Nb-rich SPP evaporating only at a higher local field than the α-Zr matrix around it, creating a protruding region of increased local curvature on the evaporating surface [45]. Previous APT experiments have analysed Nb-rich phases with a similar composition and have not reported any increase in hydrogen levels in these features (Supplementary Figs. 1 and 2) [42]. This supports the hypothesis that the difference in evaporation field between the Nb and Zr, and hence any differences in the evaporation rate of the Zr matrix and Nb-rich SPPs, is unlikely to be responsible for increased levels of detected hydrogen from this phase.

4) Surface migration during analysis of hydrogen originally present in the material

The final source of artefactual hydrogen during the experiment comes from the sample itself. Hydrogen that is present in the specimen could diffuse over the sample surface and evaporate preferentially during analysis. Whilst surface migration is likely to occur towards regions of high field [40], the migrating species can be expected to evaporate once a critical field is reached. The field in the SPP is higher than the surrounding matrix, as can be seen by the much higher $Zr^{3+}/Zr^{2+}$ ratios in the mass spectra in Fig. 2(d) ($Zr^{3+}$:$Zr^{2+}$ = 0.003 in the matrix vs 0.021 in the SPP). If hydrogen was migrating to this feature during analysis, it is highly likely that it would evaporate as the field increased in the vicinity of the SPP, leading to an enrichment of detected hydrogen around the SPP. However, the hydrogen content shows a sharp increase in the SPP in the x-y plane, Fig. 3(b), which remains consistently high across the SPP.

After consideration of these factors, we believe that the increased hydrogen levels from the β-Nb SPP is unlikely to be the result of experimental artefacts that arise during sample preparation or APT analysis. This is the first experimental observation showing preferential segregation of hydrogen to a β-Nb SPP. If Nb-rich SPPs act as sinks then it is reasonable to assume that levels of hydrogen in solution in the matrix will be lower than would be expected from the stage of the corrosion process the sample has experienced, and the formation of hydrides may be postponed. Unfortunately, due to their low number density and small size making them difficult to specifically target during sample preparation, no other SPP types were analysed during this study and so we cannot comment on the nature of the interaction of hydrogen with these other SPP types.

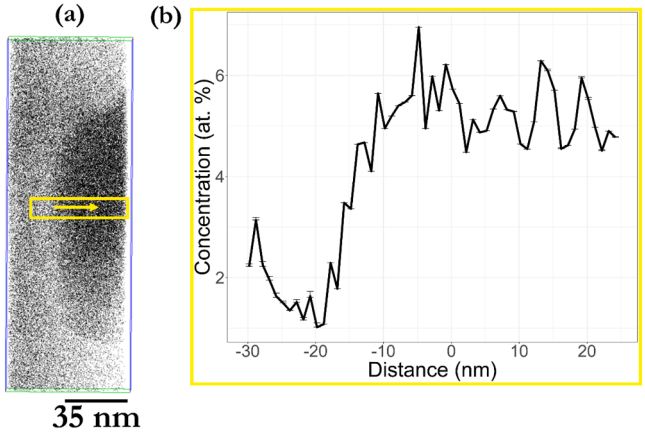


**Fig. 3.** (c) Atom map of H from region of interest highlighted by red box in Fig. 1(a) (bounding box dimensions 70 nm × 72 nm × 300 nm). (b) One-dimensional concentration profile through the region of interest indicated by the yellow box in (a). Analysis temperature = 60 K, laser pulse energy = 80 pJ. (For interpretation of the references to colour in this figure legend, the reader is referred to the web version of this article.)

### 3.2. Nb-rich nanoclusters

In addition to the large Nb-rich SPP in Fig. 1, a series of Nb-rich nanoclusters were also observed to have formed in the α-Zr grains after irradiation to 3 dpa. These are highlighted in the segment of the dataset that is displayed in Fig. 4(a) and are commonly observed in irradiated Nb-containing Zr alloys [46,47]. Fig. 4(b) shows that hydrogen also appears to be spatially correlated with some of the Nb-rich nanoclusters. To extract these features from the rest of the dataset so that their local composition could be investigated, 12 at.% Nb isosurfaces were generated to ensure that only the cores of the Nb nanoclusters were isolated for analysis. Within these Nb nanoclusters, the composition was determined to be enriched in Nb, Sn and hydrogen compared to the rest of the matrix, Table 3. Whilst the increase in Nb and Sn is far above the uncertainty in the compositional measurement, the increase in the hydrogen signal is less pronounced than it was in the β-Nb SPP. Therefore, in order to determine if this measured increase can be identified as evidence of hydrogen segregation to Nb-rich nanoclusters with compositions of approximately $Zr_3Nb$, very far from the equilibrium composition of the β-Nb phase [34], DFT modelling was performed.

Based on the APT measurements of nanocluster composition, the DFT model assumed a composition of Zr-28Nb-4Sn (at.%). The other solutes might have a significant effect on the modelled trapping behaviour of hydrogen, but they are present in such low concentrations in the nanoclusters that it is unlikely that their effect would dominate over that of the main solutes Nb and Sn and they were excluded to avoid computational complexity. Special care was taken to ensure that the supercell retained a HCP structure upon relaxation. It was noticed that in the absence of Sn, the binary Zr-Nb solid solution with Nb ≥ 16 at.% would undergo a displacive barrierless transformation, resulting in either a fully bcc structure or in a supercell with a twinned region. However, the presence of Sn stabilised the α-Zr and suppressed this phenomenon, enabling simulation of a HCP structure with a chemical composition close to that observed by APT. These simulations of Nb-rich HCP clusters complement previous DFT simulations of Nb-rich bcc phases [9] carried out using an equivalent methodology, thus enabling direct comparison.

The authors note that the DFT simulations do not account for the presence of interfaces or radiation-induced defects such as vacancies, interstitials and dislocations. Whilst irradiation will lead to an increased density of defects within the microstructure, it is currently not possible to experimentally measure their concentrations in discrete regions of the microstructure, which is required to guide the modelling. Thus, we make the assumption that radiation-induced defects are present in the α-Zr, the β-Nb SPPs, and the Nb-nanoclusters, but that their effect on H

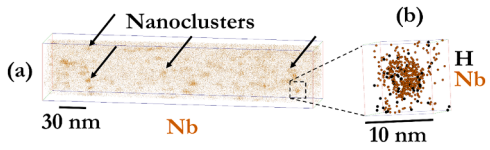


**Fig. 4.** (a) Atom map showing the distribution of Nb in a region of the sample from Fig. 1. Material is low Sn ZIRLO irradiated to 3 dpa and prepared via cryo-FIB (bounding box dimensions 63 nm x 65 nm x 300 nm). (b) Enlarged view showing spatial distribution of H and Nb within one Nb-rich nanocluster (bounding box dimensions 10 nm x 10 nm x 10 nm) Analysis temperature = 60 K, laser pulse energy = 80 pJ.

**Table 3**
Composition of the Nb-rich nanoclusters present throughout the dataset in Fig. 1. For clarity, minor elements, such as Cr and Si present in concentrations of less than 0.1 at.% are not included in the table.

| Element | Atomic% |
|---|---|
| Zr | 62.86 ± 1.76 |
| Nb | 28.67 ± 1.32 |
| H | 3.47 ± 0.89 |
| O | 0.56 ± 0.14 |
| Fe | 0.21 ± 0.08 |
| Sn | 4.07 ± 0.45 |
| Al | 0.11 ± 0.08 |

trapping is likely to be similar in each case. This view is supported by our observation that the experimentally measured hydrogen concentration in the β-Nb and Nb-nanoclusters are reasonably similar, which is in agreement with the DFT results that show there is limited difference in the trapping energies between the two regions. Indeed, the secondary effects from vacancies, interstitials, dislocations, and interfaces are either of limited importance to the results, or their effects are strong but somehow cancelling out, and coincidentally leading to the same result.

The results of the DFT simulations are presented in Fig. 5. Fig. 5(a) shows a large variance of $\Delta E^{H}_{sol,i}$ values within the Nb-rich nanoclusters, but that the median and upper and lower quartiles are all negative, indicating that hydrogen prefers to reside in interstitial sites in the Nb-nanoclusters than in interstitial sites in the α-Zr matrix. Fig. 5(b) shows the distribution in calculated solution energies as a histogram; there are some positive relative solution energies and hydrogen is unlikely to reside in these sites and will move to other, more favourable, interstitial locations. It is worth noting that interfacial strain effects might affect the bulk values calculated here.

The large variance in $\Delta E^{H}_{sol,i}$ values is likely due to the many local environments in which the interstitial hydrogen atoms can find themselves in the HCP structure. The variation of $\Delta E^{H}_{sol,i}$ as a function of nearest neighbour identity and count is presented in Fig. 5(c). It can be seen that it is highly unfavourable for the hydrogen atoms to be accommodated near Sn atoms. The presence of even one nearest neighbour of Sn increased $\Delta E^{H}_{sol,i}$ to 0.3 eV above that of HCP-Zr, and in several simulations an hydrogen atom placed near Sn was found to spontaneously relax to a site further away from Sn. Nb nearest neighbours also have an effect on $\Delta E^{H}_{sol,i}$; increasing the number of Nb nearest neighbours reduces the stability of hydrogen atoms in the interstitial sites. As a result, the most favourable interstitial sites are those surrounded only by Zr nearest neighbours. This appears counter-intuitive, as the interstitial sites surrounded only by Zr nearest neighbours in the simulated nanocluster have lower energy than the same sites in pure HCP-Zr, suggesting that Nb and Sn have an effect on the solution energy, but this effect is strongest when neither solute is nearest neighbour to hydrogen. One possible mechanism is lattice distortion caused by the solutes, leading to a wider range of accommodation site geometries, however no strong correlation was observed between solution energy and interstice volume or tetrahedral deformation. An alternative potential mechanism is that the increase in valence electrons donated by Nb solutes leads to a global reduction in hydrogen solution energy, countered locally by the distortion of smaller Nb atoms (radius 147 pm vs 161 pm of Zr).

The confidence with which hydrogen content can be measured at Nb-rich nanoclusters with APT is limited due to the small number of atoms in these features reducing the statistical counting power, as well as the various uncertainties surrounding accurate quantification of hydrogen when using APT. However, DFT modelling supports the APT observations of increased hydrogen levels at these Nb and Sn-enriched clusters. The local environment of the hydrogen interstitial was found to have a

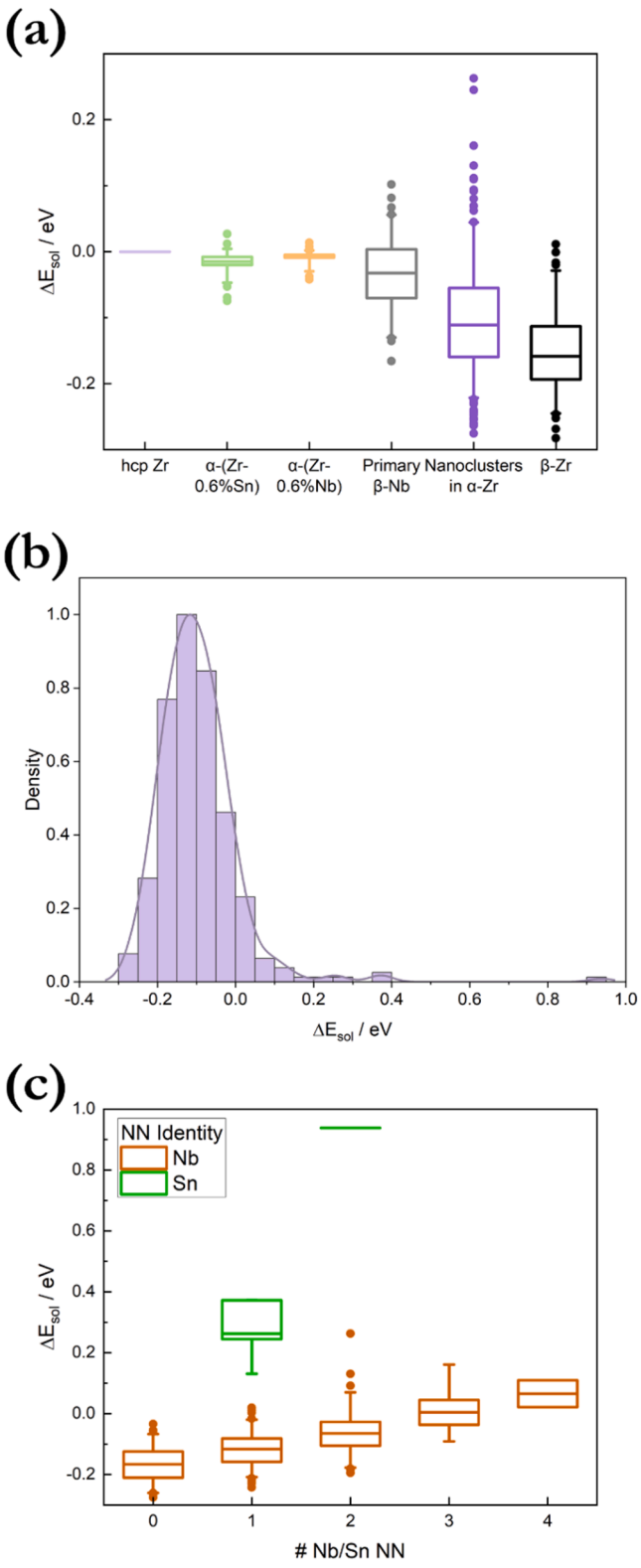


**Fig. 5.** DFT modelling results showing: (a) the distribution of H trapping energies in various microstructural regions (with comparison to results from [9]). (b) A histogram of trapping energies in Nb nanoclusters and (c) the variation of H trapping energy compared to the α-Zr matrix, as a function of the number of nearest neighbours (NN) of Sn and Nb.

big impact on its stability in the DFT simulations, with Sn and Nb nearest neighbours increasing the $\Delta E^{H}_{sol,i}$. This indicates that in neutron-irradiated Nb-containing Zr alloys, there may be new hydrogen traps being generated by the irradiation-induced nucleation of Nb-rich clusters. This is likely to affect the behaviour of hydrogen in these alloys both during and after service.

### 3.3. Summary and conclusions

The behaviour of hydrogen atoms within Zr alloys at the scale of the microstructure is of considerable interest to the nuclear materials community, but has previously been difficult to study by APT because of excess hydrogen from experimental artefacts. FIB preparation at cryogenic temperatures substantially reduces the analysed hydrogen content in Zr specimens [21], and has enabled investigation of the spatial distribution of hydrogen in a neutron-irradiated low Sn ZIRLO alloy. The APT data presented here provides evidence that a β-Nb SPP can act as a significant sink for hydrogen, and also suggests that hydrogen is present in higher concentrations in radiation-induced Nb-rich nanoclusters than in the α-Zr matrix. These results are supported by DFT modelling, which suggests that the Nb-rich nanoclusters should act as slightly stronger hydrogen sinks than bulk β-Nb SPPs. Future APT work that uses deuterium charging may permit more accurate quantification of hydrogen levels at specific features in neutron-irradiated Zr alloys.

These observations enhance our understanding of the behaviour of hydrogen in Nb-containing Zr alloys during and after service in nuclear power plants. Readers should note that since experimental observations were obtained at low temperature, caution should be exercised when extrapolating the results from this study to describe or predict the behaviour of hydrogen under operating conditions. However, how hydrogen interacts with the microstructure in zirconium at lower temperatures is also of engineering relevance, for example during extended storage of the fuel rods after service. The observation of hydrogen trapping at Nb-rich features could now be accounted for in the models used to predict hydrogen behaviour in zirconium-based alloys.

## CRediT authorship contribution statement

**Benjamin M. Jenkins:** Conceptualization, Methodology, Formal analysis, Investigation, Writing – original draft. **Jack Haley:** Conceptualization, Methodology, Investigation, Writing – review & editing. **Lucia Chen:** Formal analysis, Investigation, Writing – review & editing. **Baptiste Gault:** Validation, Writing – review & editing. **Patrick A. Burr:** Formal analysis, Investigation, Writing – review & editing. **Anne Callow:** Formal analysis, Investigation, Writing – review & editing. **Michael P. Moody:** Writing – review & editing, Funding acquisition. **Christopher R.M. Grovenor:** Conceptualization, Writing – review & editing, Funding acquisition.

## Declaration of Competing Interest

The authors declare that they have no known competing financial interests or personal relationships that could have appeared to influence the work reported in this paper.

## Data availability

Data will be made available on request.

## Acknowledgements

The atom probe facilities at the University of Oxford are funded by the Engineering and Physical Sciences Research Council (EPSRC) grants EP/M022803/1 and EP/T011505/1. The research used UKAEA's Materials Research Facility, which has been funded by and is part of the UK's National Nuclear User Facility and Henry Royce Institute for Advanced Materials (EP/R00661X/1). BMJ and JH would like to acknowledge funding from EPSRC program grant MIDAS (EP/S01702X/1) for the study of irradiation damage in zirconium alloys. This research was part funded under the £46 m Advanced Fuel Cycle Programme (AFCP) as part of the Department for Business, Energy and Industrial Strategy's (BEIS) £505 m Energy Innovation Programme and the TEM at National Nuclear Laboratory was funded by EPSRC grant EP/I034106/1. BMJ is a recipient of the WINNINGNormandy Program supported by the Normandy Region and would like to acknowledge this project has received funding from the European Union's Horizon 2020 research and innovation programme under the Marie Sklodowska Curie grant agreement No. 101034329.

## Supplementary materials

Supplementary material associated with this article can be found, in the online version, at doi:10.1016/j.jnucmat.2023.154755.

## References

[1] S. Kass, Hydrogen pickup in various zirconium alloys during corrosion exposure in high-temperature water and steam, J. Electrochem. Soc. 107 (1960) 594, https://doi.org/10.1149/1.2427781.
[2] A.T. Motta, A. Couet, R.J. Comstock, Corrosion of zirconium alloys used for nuclear fuel cladding, Annu. Rev. Mater. Res. 45 (2015) 311–343, https://doi.org/10.1146/annurev-matsci-070214-020951.
[3] A.T. Motta, L. Capolungo, L.Q. Chen, M.N. Cinbiz, M.R. Daymond, D.A. Koss, E. Lacroix, G. Pastore, P.C.A. Simon, M.R. Tonks, B.D. Wirth, M.A. Zikry, Hydrogen in zirconium alloys: a review, J. Nucl. Mater. 518 (2019) 440–460, https://doi.org/10.1016/j.jnucmat.2019.02.042.
[4] J.J. Kearns, Terminal solubility and partitioning of hydrogen in the alpha phase of zirconium, Zircaloy-2 and Zircaloy-4, J. Nucl. Mater. 22 (1967) 292–303, https://doi.org/10.1016/0022-3115(67)90047-5.
[5] I. Mouton, Y. Chang, P. Chakraborty, S. Wang, L.T. Stephenson, T.B. Britton, B. Gault, Hydride growth mechanism in Zircaloy-4: investigation of the partitioning of alloying elements, Materialia (2021) 15, https://doi.org/10.1016/j.mtla.2021.101006.
[6] S. Suman, M.K. Khan, M. Pathak, R.N. Singh, J.K. Chakravartty, Hydrogen in Zircaloy: mechanism and its impacts, Int. J. Hydrogen Energy 40 (2015) 5976–5994, https://doi.org/10.1016/j.ijhydene.2015.03.049.
[7] H.K.D.H. Bhadeshia, Prevention of Hydrogen Embrittlement in Steels, ISIJ Int. 56 (2016) 24–36, https://doi.org/10.2355/isijinternational.ISIJINT-2015-430.
[8] P.A. Burr, S.T. Murphy, S.C. Lumley, M.R. Wenman, R.W. Grimes, Hydrogen solubility in zirconium intermetallic second phase particles, J. Nucl. Mater. 443 (2013) 502–506, https://doi.org/10.1016/j.jnucmat.2013.07.060.
[9] V. Tuli, A. Claisse, P.A. Burr, Hydrogen solubility in Zr–Nb alloys, Scr. Mater. 214 (2022), 114652, https://doi.org/10.1016/j.scriptamat.2022.114652.
[10] C. Jones, V. Tuli, Z. Shah, M. Gass, P.A. Burr, M. Preuss, K.L. Moore, Evidence of hydrogen trapping at second phase particles in zirconium alloys, Sci. Rep. 11 (2021) 1–12, https://doi.org/10.1038/s41598-021-83859-w.
[11] J. Takahashi, K. Kawakami, Y. Kobayashi, T. Tarui, The first direct observation of hydrogen trapping sites in TiC precipitation-hardening steel through atom probe tomography, Scr. Mater. 63 (2010) 261–264, https://doi.org/10.1016/j.scriptamat.2010.03.012.
[12] D. Haley, S.V. Merzlikin, P. Choi, D. Raabe, Atom probe tomography observation of hydrogen in high-Mn steel and silver charged via an electrolytic route, Int. J. Hydrogen Energy 39 (2014) 12221–12229, https://doi.org/10.1016/j.ijhydene.2014.05.169.
[13] Y.S. Chen, D. Haley, S.S.A. Gerstl, A.J. London, F. Sweeney, R.A. Wepf, W. M. Rainforth, P.A.J. Bagot, M.P. Moody, Direct observation of individual hydrogen atoms at trapping sites in a ferritic steel, Science 355 (2017) 1196–1199, https://doi.org/10.1126/science.aal2418.
[14] M.S. Meier, M.E. Jones, P.J. Felfer, M.P. Moody, D. Haley, Extending estimating hydrogen content in atom probe tomography experiments where $H_2$ molecule formation occurs, Microsc. Microanal. (2021) 1–14, https://doi.org/10.1017/S1431927621012332.
[15] J. Takahashi, K. Kawakami, T. Tarui, Direct observation of hydrogen-trapping sites in vanadium carbide precipitation steel by atom probe tomography, Scr. Mater. 67 (2012) 213–216, https://doi.org/10.1016/j.scriptamat.2012.04.022.
[16] I. Mouton, A.J. Breen, S. Wang, Y. Chang, A. Szczepaniak, P. Kontis, L. T. Stephenson, D. Raabe, M. Herbig, T.B. Britton, B. Gault, Quantification challenges for atom probe tomography of hydrogen and deuterium in zircaloy-4, Microsc. Microanal. 25 (2019) 481–488, https://doi.org/10.1017/S143192761801615X.
[17] M.E. Jones, A.J. London, A.J. Breen, P.D. Styman, S. Sikotra, M.P. Moody, D. Haley, Improving the quantification of deuterium in zirconium alloy atom probe

tomography data using existing analysis methods, Microsc. Microanal. (2021) 1–10, https://doi.org/10.1017/S1431927621012848.
[18] D. Banerjee, C.G. Shelton, B. Ralph, J.C. Williams, A resolution of the interface phase problem in titanium alloys, Acta Metall. 36 (1988) 125–141, https://doi.org/10.1016/0001-6160(88)90033-8.
[19] R. Ding, I.P. Jones, In situ hydride formation in titanium during focused ion milling, J. Electron. Microsc. (Tokyo) 60 (2011) 1–9, https://doi.org/10.1093/jmicro/dfq066.
[20] Y. Chang, W. Lu, J. Guénolé, L.T. Stephenson, A. Szczpaniak, P. Kontis, A. K. Ackerman, F.F. Dear, I. Mouton, X. Zhong, S. Zhang, D. Dye, C.H. Liebscher, D. Ponge, S. Korte-Kerzel, D. Raabe, B. Gault, Ti and its alloys as examples of cryogenic focused ion beam milling of environmentally-sensitive materials, Nat. Commun. 10 (2019) 1–10, https://doi.org/10.1038/s41467-019-08752-7.
[21] S.M. Hanlon, S.Y. Persaud, F. Long, A. Korinek, M.R. Daymond, A solution to FIB induced artefact hydrides in Zr alloys, J. Nucl. Mater. 515 (2019) 122–134, https://doi.org/10.1016/j.jnucmat.2018.12.020.
[22] D. Mayweg, J. Eriksson, O. Bäcke, A.J. Breen, M. Thuvander, Focused Ion Beam induced hydride formation does not affect Fe, Ni, Cr-clusters in irradiated Zircaloy-2, J. Nucl. Mater. 581 (2023), 154444, https://doi.org/10.1016/j.jnucmat.2023.154444.
[23] B.M. Jenkins, J. Haley, M.P. Moody, J.M. Hyde, C.R.M. Grovenor, APT and TEM study of behaviour of alloying elements in neutron-irradiated zirconium-based alloys, Scr. Mater. 208 (2022), 114323, https://doi.org/10.1016/j.scriptamat.2021.114323.
[24] S. Yagnik, R.B. Adamson, G. Kobylyansky, J.H. Chen, D. Gilbon, S. Ishimoto, T. Fukuda, L. Hallstadius, A. Obukhov, S. Mahmood, Effect of alloying elements, cold work, and hydrogen on the irradiation-induced growth behavior of zirconium alloy variants, ASTM Spec. Tech. Public. STP 1597 (2018) 748–795, https://doi.org/10.1520/STP159720160040.
[25] K. Thompson, D. Lawrence, D.J. Larson, J.D. Olson, T.F. Kelly, B. Gorman, In situ site-specific specimen preparation for atom probe tomography, Ultramicroscopy 107 (2007) 131–139, https://doi.org/10.1016/j.ultramic.2006.06.008.
[26] M.K. Miller, K.F. Russell, G.B. Thompson, Strategies for fabricating atom probe specimens with a dual beam FIB, Ultramicroscopy 102 (2005) 287–298, https://doi.org/10.1016/j.ultramic.2004.10.011.
[27] L.A. Giannuzzi, J.L. Drown, S.R. Brown, R.B. Irwin, F.A. Stevie, Applications of the FIB lift-out technique for TEM specimen preparation, Microsc. Res. Tech. 41 (1998) 285–290, https://doi.org/10.1002/(SICI)1097-0029(19980515)41:4<285::AID-JEMT1>3.0.CO;2-Q.
[28] A.J. London, AtomProbeLab, (2019) https://sourceforge.net/projects/atomprobelab/. https://sourceforge.net/projects/atomprobelab/.
[29] A.J. London, Quantifying uncertainty from mass-peak overlaps in atom probe microscopy, Microsc. Microanal. (2019) 1–11, https://doi.org/10.1017/S1431927618016276.
[30] A. Van De Walle, P. Tiwary, M. De Jong, D.L. Olmsted, M. Asta, A. Dick, D. Shin, Y. Wang, L.Q. Chen, Z.K. Liu, Efficient stochastic generation of special quasirandom structures, Calphad: Comput. Coupl. Phase Diagr. Thermochem. 42 (2013) 13–18, https://doi.org/10.1016/j.calphad.2013.06.006.
[31] G. Kresse, J. Furthmüller, Efficient iterative schemes for ab initio total-energy calculations using a plane-wave basis set, Phys. Rev. B - Condens. Matter Mater. Phys. 54 (1996) 11169–11186, https://doi.org/10.1103/PhysRevB.54.11169.
[32] J.P. Perdew, K. Burke, M. Ernzerhof, Generalized gradient approximation made simple, Phys. Rev. Lett. 77 (1996) 3865–3868, https://doi.org/10.1103/PhysRevLett.77.3865.
[33] G. He, J. Liu, K. Li, J. Hu, A.H. Mir, S. Lozano-Perez, C. Grovenor, Investigating the stability of second phase particles in Zr-Nb alloys under irradiation, J. Nucl. Mater. 526 (2019), 151738, https://doi.org/10.1016/j.jnucmat.2019.151738.
[34] A. Harte, M. Griffiths, M. Preuss, The characterisation of second phases in the Zr-Nb and Zr-Nb-Sn-Fe alloys: a critical review, J. Nucl. Mater. 505 (2018) 227–239, https://doi.org/10.1016/j.jnucmat.2018.03.030.
[35] S.H. Yoo, S.H. Kim, E. Woods, B. Gault, M. Todorova, J. Neugebauer, Origins of the hydrogen signal in atom probe tomography: case studies of alkali and noble metals, New J. Phys. (2022) 24, https://doi.org/10.1088/1367-2630/ac40cd.
[36] V.N. Shishov, M.M. Peregud, A.V. Nikulina, P.V. Shebaldov, A.V. Tselischev, A. E. Novoselov, G.P. Kobylyansky, Z.E. Ostrovsky, V.K. Shamardin, Influence of zirconium alloy chemical composition on microstructure formation and irradiation induced growth, ASTM Spec. Tech. Publ. (2002) 758–778, https://doi.org/10.1520/stp11415s.
[37] G. Sha, A. Cerezo, G.D.W. Smith, Field evaporation behavior during irradiation with picosecond laser pulses, Appl. Phys. Lett. 92 (2008), https://doi.org/10.1063/1.2837626, 043503-1-043503–3.
[38] D.R. Kingham, The post-ionization of field evaporated ions: a theoretical explanation of multiple charge states, Surf. Sci. 116 (1982) 273–301, https://doi.org/10.1016/0039-6028(82)90434-4.
[39] T.T. Tsong, T.J. Kinkus, C.F. Ai, Field induced and surface catalyzed formation of novel ions: a pulsed-laser time-of-flight atom-probe study, J. Chem. Phys. 78 (1983) 4763–4775, https://doi.org/10.1063/1.445276.
[40] B. Gault, F. Danoix, K. Hoummada, D. Mangelinck, H. Leitner, Impact of directional walk on atom probe microanalysis, Ultramicroscopy 113 (2012) 182–191, https://doi.org/10.1016/j.ultramic.2011.06.005.
[41] E.M. Francis, A. Harte, P. Frankel, S.J. Haigh, D. Jädernäs, J. Romero, L. Hallstadius, M. Preuss, Iron redistribution in a zirconium alloy after neutron and proton irradiation studied by energy-dispersive X-ray spectroscopy (EDX) using an aberration-corrected (scanning) transmission electron microscope, J. Nucl. Mater. 454 (2014) 387–397, https://doi.org/10.1016/j.jnucmat.2014.08.034.
[42] A. Callow, Atom Probe Tomography of Irradiated Zirconium Alloys, University of Oxford, 2021. https://ora.ox.ac.uk/objects/uuid:f31d8cdf-cbf8-45ae-a107-8b1921ad7194.
[43] G. Sundell, M. Thuvander, H.O. Andrén, Hydrogen analysis in APT: methods to control adsorption and dissociation of H2, Ultramicroscopy 132 (2013) 285–289, https://doi.org/10.1016/j.ultramic.2013.01.007.
[44] P. Felfer, B. Ott, M. Monajem, V. Dalbauer, M. Heller, J. Josten, C. Macaulay, An Atom Probe with Ultra-Low Hydrogen Background, Microsc. Microanal. (2021) 1–9, https://doi.org/10.1017/S1431927621013702.
[45] B. Gault, M.P. Moody, J.M. Cairney, S.P. Ringer, Atom Probe Microscopy, Springer-Verlag, New York, 2012.
[46] J. Ribis, S. Doriot, F. Onimus, Shape, orientation relationships and interface structure of beta-Nb nano-particles in neutron irradiated zirconium alloy, J. Nucl. Mater. 511 (2018) 18–29, https://doi.org/10.1016/j.jnucmat.2018.08.042.
[47] G. He, Radiation Damage and Its Impact On Corrosion in Zirconium-Niobium alloys - thesis, University of Oxford, 2020. https://ora.ox.ac.uk/objects/uuid:e25658ad-3d32-4e72-9399-99542429a5a2.